Thermal structure, radial anisotropy, and dynamics of oceanic boundary layers

Ludwig Auer, Thorsten W. Becker, Lapo Boschi, Nicholas C. Schmerr

Thermal structure, radial anisotropy, and dynamics of oceanic boundary layers

Ludwig Auer[1], Thorsten W. Becker[2], Lapo Boschi[3,4] and Nicholas Schmerr[5]

Corresponding author: Ludwig Auer, Institut für Geophysik, Eidgenössische Technische Hochschule Zürich, Zürich, Switzerland (ludwig.auer@tomo.ig.erdw.ethz.ch)

[1]Institut für Geophysik, Eidgenössische

Oceanic lithosphere when defined as a thermal boundary layer explains bathymetry and isotropic wavespeeds to first order. In contrast, SS precursors and receiver functions suggest a subhorizontal interface of unclear origin within this layer, on top of a radially anisotropic zone. Here, we study the relationships between discontinuities, lithospheric thickness, and anisotropy by testing a suite of geodynamic scenarios. We find that strong age-dependency of the radially anisotropic zone is inconsistent with models and observations, and that a weaker discontinuity confines the zone from below. While azimuthal anisotropy is consistent with lattice preferred orientation of olivine due to

Technische Hochschule Zürich, Zürich, Switzerland

[2]Department of Earth Sciences, University of Southern California, Los Angeles, USA

[3]Sorbonne Universites, UPMC Univ Paris 06, UMR 7193, Institut des Sciences de la Terre Paris (iSTeP), F-75005 Paris, France.

[4]CNRS, UMR 7193, Institut des Sciences de la Terre Paris (iSTeP), F-75005 Paris, France

[5]Department of Geology, University of Maryland, College Park, USA

asthenospheric flow underneath the lithosphere, radial anisotropy might require additional contributions from petrological fabrics or melt ponding. This implies that reflectors previously associated with the base of the lithosphere are instead associated with preserved structures embedded in it. They carry information about plate formation, but have little control on plate deformation.

1. Introduction

The oceanic lithosphere can be understood as the rheological manifestation of a thermal boundary layer that forms at the mid-ocean spreading centers and grows thicker as the newly formed plate is carried away, thus having more time to cool down to larger depths. The underlying asthenosphere is warmer, hence more ductile and separated by a rheological transition region from the mechanically stronger lithosphere. This thermo-mechanical definition of the lithosphere is supported by bathymetry [e.g. *Zhong et al.*, 2007], depth dependence of seismicity [e.g. *Chen and Molnar*, 1983; *McKenzie et al.*, 2005], effective elastic thickness variations [e.g. *Watts et al.*, 2013], and isotropic shear-velocity (v_S) structure which conform to half-space cooling (HSC), to first order [e.g. *Ritzwoller et al.*, 2004].

The thermal influence on isotropic upper-mantle velocity structure can be visualized by referencing shear-velocity anomalies from tomography models against sea-floor ages [e.g. *Priestley and McKenzie*, 2013]. Such analysis based on the isotropic component of the global shear-velocity model *savani* [*Auer et al.*, 2014] and ages from *Müller et al.* [2008] (Fig. 1) compares well with estimates from half-space cooling; see, for example, the deeper green line in Figs. 1a-b, where an an asthenospheric temperature of 1315°C and a temperature-dependent conductivity was used [cf. *McKenzie et al.*, 2005] for the Pacific and Atlantic domains, with regions defined as shown in Fig. S1. For the Atlantic, for example, the oceanic upper mantle broadly agrees with the half-space cooling paradigm in the sense that the 4.4 km/s wave-speed contour approximately aligns with the 1200°C HSC isotherm.

Upper-mantle seismic anisotropy can also be imaged with seismic tomography and provides further constraints on boundary layer dynamics [e.g. *Long and Becker*, 2010]. Two forms of anisotropy are typically constrained: i), radial anisotropy, quantified as the ratio between the velocity of horizontally traveling, horizontally polarized shear waves, v_{SH}, and the velocity of horizontally traveling, vertically polarized shear waves, v_{SV}, and, ii), azimuthal anisotropy, i.e. hexagonal anisotropy with a horizontal symmetry axis, invoked to model the azimuthal dependence of surface-wave phase velocities. Azimuthal anisotropy is present in the oceanic lithosphere and uppermost asthenosphere [e.g. *Ekström*, 2011; *Burgos et al.*, 2014], and was recently shown to be consistent with a thermally controlled lithosphere under which shear forms anisotropy via lattice-preferred orientation (LPO) of intrinsically anisotropic minerals [*Becker et al.*, 2014; *Beghein et al.*, 2014].

Radial anisotropy in the upper mantle is most pronounced underneath the Central Pacific and generally described as an anomalous layer of increased $v_{SH} > v_{SV}$ having a thickness of $80 - 100$ km [e.g., *Ekström and Dziewonski*, 1998; *Boschi and Ekström*, 2002; *French et al.*, 2013; *Burgos et al.*, 2014; *Beghein et al.*, 2014; *Auer et al.*, 2014], a smooth upper and lower onset gradient, and a peak at approximately 100 to 120 km (with some tomography models showing it extending to depths greater than 200 km; see, e.g., Fig. 2e in *Beghein et al.* [2014]). Importantly, this radially anisotropic anomaly appears structurally decoupled from azimuthal anisotropy and its upper bound is significantly flatter than what HSC-related structure would imply, as shown in Fig. 2 (top left panel), where the anisotropic component of *savani* [*Auer et al.*, 2014], given in terms of $\xi = v_{SH}^2/v_{SV}^2$, is referenced against ages under the Pacific. This observation is consistent with

recent work by *Burgos et al.* [2014] and *Beghein et al.* [2014]. Yet, earlier studies had reported weak age dependency of the radially anisotropic layer [*Nettles and Dziewoński*, 2008; *Kustowski et al.*, 2008].

Analysis of body-wave receiver functions as well as short- and long-period SS precursors provide further means to probe the uppermost mantle and to detect seismic discontinuities [e.g., *Kawakatsu et al.*, 2009; *Kumar and Kawakatsu*, 2011; *Rychert and Shearer*, 2011; *Schmerr*, 2012]. The different types of measurements indicate a relatively sharp negative velocity contrast underneath the oceans at an average depth of $\sim$ 60 km [*Kumar and Kawakatsu*, 2011; *Schmerr*, 2012], which is often identified with the oceanic Gutenberg discontinuity or G [cf. *Gutenberg*, 1926]. The *Kumar and Kawakatsu* [2011] receiver function estimate of G depth is only weakly proportional to sea-floor age. *Schmerr* [2012] also notes a subtle age dependency, much weaker than what is expected from purely thermal control. In contrast, *Rychert and Shearer* [2011] found age-dependent depth variations between 25 and 130 km for their long-period SS-based interfaces. A comprehensive compilation of various attempts to map upper-mantle discontinuities, and associated inconsistencies across the different datasets are discussed by *Rychert et al.* [2012].

Superimposing the interface estimates of *Schmerr* [2012] and *Kumar and Kawakatsu* [2011] upon the ξ-component of *savani* (Fig. 2, top left panel), the similarity between the upper boundary of the high-ξ zone and the Gutenberg discontinuity ($\sim$ 60 km) becomes apparent [*Beghein et al.*, 2014]. Based on the complete dataset of *Schmerr* [2012], we also identify a similar (albeit weaker), deeper interface to approximately coincide with the lower boundary of the high-ξ zone at a depth of $\sim$ 150 km. An equivalent discontinuity

is present in the anisotropic component of the regionalized 1-D models $PHB3$ and $PA5$ (see the black lines in Fig. 2) which are obtained along age corridors of $\sim$ 50 Ma and $\sim$ 120 Ma, in the Philippine Sea and the Central Pacific Ocean, respectively [*Gaherty et al.*, 1996, 1999], and are here superimposed on the Pacific regionalization of Fig. 2 for illustrative purposes.

Thus it appears that different seismological observations point to different inferences regarding the structure of oceanic lithosphere and its relation to temperature, leading to the obvious question of whether the bulk of the observed radial anisotropy is a direct consequence of plate-induced shearing, whether there is significant contribution from other mechanisms [*Karato*, 2012; *Beghein et al.*, 2014; *Burgos et al.*, 2014; *Becker et al.*, 2014], or whether there are simply resolution issues that prevent a correct interpretation.

One of the issues that potentially influence model resolution is related to tomographic inverse problems being mixed-determined and as such requiring regularization. Regularization involves subjective choices left to the discretion of the tomographer and can introduce artificial smoothing of seismic images [e.g. *Boschi and Dziewoński*, 1999]. In particular, regularization schemes that "smooth" tomographic images might, depending on a model's vertical and horizontal resolution, mask the signature of lithospheric age, and favor age-independent models. Here, we circumvent such issues by conducting only "forward" calculations for conceptual shear-velocity models that are based both on geodynamics and tomography, and measure how well they fit seismic data, thereby evaluating the robustness of tomography-based observations of age-independent radially anisotropic

anomalies. Subsequently, we reconcile our new results with additional seismological and mineralogical constraints for a new unified model of the oceanic uppermost mantle.

2. Geodynamic hypothesis tests

2.1. Method and data

Our experiments follow the probabilistic approach advocated by *Tarantola* [2006], and are based on the idea that instead of the inverting data to arrive at one best solution, it is to be preferred to invent models based on intuition and prior knowledge and falsify them against a dataset, to pass from a prior to a posterior collection of admissible solutions.

Our geodynamic-seismological model hypotheses are designed to reflect the key (and most robust) features observed in tomographic images as well as the a-priori structure one would expect from fundamental geodynamic considerations. Given that global v_S structure is resolved much better than global anisotropic structure [e.g. *Becker et al.*, 2008; *Auer et al.*, 2014], the isotropic component of all forward tests is fixed to a 3-D background model, based on the surface-wave overtone (OT) and fundamental mode (FM) dispersion datasets, already used in *Auer et al.* [2014]. This new model is optimized for high vertical resolution and covers the upper 400 km of the mantle, hereafter referred to as $savanUM$. $SavanUM$ is largely consistent with its whole-mantle counterpart *savani* but exhibits higher ξ amplitudes and a steeper gradient at the top of the anisotropic layer (Fig. 2). A comparison of anisotropic and isotropic structure between *savani*, $savanUM$ and the model $SEMum2$ [*French et al.*, 2013] is provided in Figs. S2 and S3.

Continental radial anisotropy in the geodynamic forward hypothesis tests is prescribed to the layer average of $savanUM$'s continental ξ to focus on the effect of oceanic structure

alone. Radial anisotropy underneath oceans is restricted to vary by only a few geodynamically motivated parameters.

The geodynamic models are first constructed in terms of the parameter ξ and $\delta v_S = \frac{\Delta v_S}{v_S}$ on a $1^\circ \times 1^\circ$ regular grid and then changed to a tomographic parameterization, by converting to δv_{SV} and δv_{SH} and projecting onto a coarser equal-area ($5^\circ \times 5^\circ$ at the equator) voxel mesh, comprising 70 layers (resulting in a total of $n = 278,320$ grid cells covering the uppermost mantle). We next compute ray-theoretical sensitivity functions [see *Auer et al.*, 2014, Fig. 1a] w.r.t. the 3-D crustal model CRUST2.0 [*Bassin et al.*, 2000] on top of the 1-D reference model PREM [*Dziewoński and Anderson*, 1981] to set up the forward problem that allows computing synthetic surface-wave phase delays for three-dimensional structural models based on our geodynamic hypotheses. The forward problem is solved via a simple dot product between the linear system matrix $\mathbf{A}$ and the coefficient vector $\mathbf{x}_{syn}$ (as defined in sec. 2.4 of *Auer et al.* [2014]) that describes our conceptual model. Different values for the geodynamic parameters that control the distribution of ξ are explored, while the data fit is monitored. A summary of varied parameters is given in Table S2. As a misfit criterion we use the variance reduction, VR, defined as

$$VR = 1 - \frac{|\mathbf{A} \cdot \mathbf{x}_{syn} - \mathbf{d_{obs}}|}{|\mathbf{d}_{obs}|} \tag{1}$$

where $\mathbf{d}_{obs}$ is a vector with the measured phase anomalies.

We employ the exact same FM and OT surface-wave measurements as *Auer et al.* [2014] but partition the global dataset in three subsets for the Pacific, the Indian and the Atlantic Ocean, by extracting ray paths that are exclusively spanning the different oceanic regions

(using the same geographical polygons employed in the regionalized age referencing) with the requirement that the recording stations be located close to the coast, such to avoid influence from continental regions.

2.2. Age-independent geodynamic hypotheses

We first consider the hypothesis that the anisotropic zone extends across the entire oceanic region and is completely independent of sea-floor age. Vertically, the strength of anisotropy $\xi(z)$ is prescribed to follow a Gaussian, defined here as

$$\xi(z) = \xi_{max} \exp\left(-\frac{(z-z_0)^2}{2\sigma^2}\right) \tag{2}$$

encapsulating the anisotropy amplitude factor ξ_{max}, the depth z, the layer offset depth z_0, and the standard deviation $\sigma \approx h/2.35482$, absorbing the half-width at half maximum h which we select as the parameter controlling the thickness of the zone. We fix h at 90 km (read off from Fig. 2) and perform a grid search over the peak amplitude ξ_{max}, varied in increments of 0.005 between 1 (no anisotropy) and 1.2, and the layer offset depth z_0, varied between zero and 230 km in 5 km steps.

Monitoring the VR associated with the model hypotheses allows us to identify, to first order, an optimal set of parameters for ξ_{max} and z_0 and the different oceans (Fig. 3a). Our results confirm that oceanic radial anisotropy is essential to fit surface-wave datasets, and show that best-fit values for depth and strength of anisotropy can be roughly identified. To derive confidence intervals for these estimates, we normalize the VR between zero and 100%, least-squares fit a multi-variate 2D Gaussian to the cropped upper 10% of the misfit-contours, and define the error intervals ($\sigma_{\xi_{max}}$ and σ_{z_0}) according to the ellipse described

by the 99% iso-contour of the Gaussian (see the black error ellipse in Fig. 3a). The results for the different oceans are similar in terms of the general shape of the misfit contours but yield different best-fit depths, anisotropy strengths and misfits. The summary given in Table S1 shows that the Pacific data subset prefers the anisotropic zone to be slightly deeper and stronger compared to the Indian and the Atlantic datasets, at z_0 of ≈ 110 km and 80 km and ξ_{max} of 1.1 and 1.07 for Pacific and Atlantic, respectively (Table S1). This suggests intra-oceanic differences, perhaps related to differences in spreading rate, and is consistent with the geodynamic estimates of *Becker et al.* [2008] (Fig. S6).

Fig. 3a compares the flat anisotropy layer depth and strength for the Pacific with approximate estimates of ξ from dry, "A" type [*Karato et al.*, 2008] LPO experiments of *Hansen et al.* [2014] (from full saturation as of their Fig. 7) for a range of pyroxene contents, and the synthetic LPO models for 30% enstatite [*Becker et al.*, 2006] of *Becker et al.* [2008]. Assuming perfect alignment in the horizontal, the laboratory LPO estimates are broadly compatible with the imaged ξ amplitudes for realistic pyroxene fractions.

Having identified a set of best-fit offset depths and the anisotropy peak amplitudes, we perform an additional two-dimensional grid search in which the center depth is fixed, to assess trade-offs between thickness and peak amplitude of the zone. As shown in Fig. S5, the VR surface less clearly plateaus at a certain best-fit set of parameters, which shows that thickness and peak amplitude significantly trade-off with each other, manifesting in a rather broad zone of different combinations of ξ_{max} peak amplitudes and thicknesses h (corresponding to similar total anisotropy "strength") that achieve almost the same data-misfits. While, for convenience, we present "best-fit" layer models for the different

oceans, our results will depend on assumptions such as isotropic structure and theoretical simplifications. Hence, relative variations of best-fit parameters are more meaningful than absolute values.

These uncertainties notwithstanding, we compare the best-fit layer model depth and thickness for the Pacific Ocean with the body wave interface estimates from reflections in Fig. 2 (bottom left panel) [*Schmerr*, 2012]. Instead of the raw interface estimates, we here bin the lower and the upper bounce depths in bins of 10 Ma and represent the data in each bin via Gaussians. Where too few measurements are available, a dot-marker is plotted at the mean depth, instead. Through the mean depths we fit a spline function, facilitating a visual comparison of the model and the bounce depths. With the exception of region at ~ 110 Myr, the match between both top and bottom reflections and the flat layer radial anisotropy model is apparent.

2.3. Age-dependent geodynamic hypotheses

We next test whether age-dependent vs. age-independent models can be discriminated by our regionalized datasets. To this end, we construct models that follow the half-space cooling solution

$$T' = \frac{T - T_0}{T_1 - T_0} = \mathrm{erf}\left(\frac{z}{2\sqrt{\kappa\tau}}\right), \tag{3}$$

where T_0 is the surface temperature, T_1 is the asthenospheric temperature, T is temperature, τ is the age, and κ is the thermal diffusivity [*Turcotte and Schubert*, 2002]. Evaluating this equation for explicit choices of T', one obtains the lithospheric thickness

$$z_L = c\sqrt{\kappa\tau}, \tag{4}$$

where $c = 2 \cdot \mathrm{erf}^{-1}(T')$. The temperature dependent κ isotherms for 1200°C of Fig. 1 can be approximated with a mantle temperature T_1 of 1315°C, a surface temperature T_0 of 14°C and a constant κ of 10^{-6} m^2/s, leading to a c of roughly 2.5. An age-dependent model of ξ is constructed via eq. (2) as above, but setting the offset depth to

$$z_1 = a + c\sqrt{\kappa\hat{\tau}(\mathbf{x}, f)} \tag{5}$$

at location $\mathbf{x}$, where eq. (5) approximates models that flatten out after a certain age: c still controls the slope of the thickness curve and a defines the Gaussian's offset depth at the spreading center. The parameter a is chosen such that z_1, averaged over the ocean under investigation, is equal to the best fit layer depth that has been found in the age-independent experiment shown in Fig. 2a. The function $\hat{\tau}$ is given by

$$\hat{\tau}(\mathbf{x}, f) = \begin{cases} \tau(\mathbf{x}) & \text{for } \tau(\mathbf{x}) < f \\ f & \text{for } \tau(\mathbf{x}) \geq f \end{cases} \tag{6}$$

where $\tau(\mathbf{x})$ are the spatially dependent ages from *Müller et al.* [2008]. This parameterization allows us to vary between age-independent end-member ξ models (i.e. the flat layer cases, with the age factor $c \to 0$ or the flattening age $f \to 0$) and age-dependent models following different half-space cooling isotherms and turning flat at larger ages.

We again perform a two-dimensional grid search, now over the parameters c and f, keeping h at 90 km and z_0 fixed at the best-fit value found for the flat layer case. We vary c in a relevant range from zero to ~ 7. Fig. 3b for the Pacific shows, that for a fixed

average depth of 110 km, misfits generally increase when transforming from flat ($c = 0$) to different age slopes ($c \to 7$). For the global dataset, misfits show the same behavior, qualitatively. For young flattening ages $f < 40$, however, there is no significant increase in misfit for higher values of c, delineating a range of weakly age dependent models which explain the data equally well.

We illustrate the results via two particulars (Fig. 3b), model B with a half-space cooling type of age-dependence but flattening at $f = 70$ Ma, and model A with the full age-dependence one would expect from the 1200°C HSC isotherm [*Becker et al.*, 2014]. As indicated by their position in the misfit contour map, model A fits the data worse, confirming that strong age-dependence is not an ideal model for the radially anisotropic anomaly. The "roughness" of our conceptual models (black contours in Fig. 3b) reflects their lateral and vertical continuity and shows that age-independent hypotheses are systematically smoother, as anticipated. This highlights that tomographic inversions regularized via roughness damping can be biased towards age-independent models.

3. Discussion

A purely geological age and HSC controlled lithosphere-asthenosphere system would predict a diffuse and strongly age-dependent lithosphere-asthenosphere transition, in contrast to our findings. Half-space cooling is, of course, only an approximation and thermal boundary layer structure deviations from a single, global HSC model may explain parts of the anisotropic complexity. Variations between ocean basins can be highlighted by the difference between the Pacific and Atlantic in terms of isotropic velocity structure (Fig. 1c). There is a clear average velocity offset, which can be interpreted as the Pa-

cific having a hotter asthenosphere than the Atlantic [cf. *Dalton et al.*, 2014], perhaps because of temporarily reduced mixing efficiency due to the slab curtains which appear to presently surround the Pacific [*Huang and Zhong*, 2005]. Along with faster spreading rates, this may lead to relatively higher degrees of partial melting under the Pacific spreading-centers, possibly explaining the localized slow anomaly at shallow depth for ages younger than $\sim$ 20 Myr in Fig. 1c. Another relative velocity anomaly is localized at sea-floor ages of around 80 Ma, where bathymetry indicates deviations from HSC [e.g. *Marty and Cazenave*, 1989; *Zhong et al.*, 2007]. For the Pacific, such deviations can be explained with thermal age resetting [*Nagihara et al.*, 1996; *Ritzwoller et al.*, 2004], whose dynamical cause is unclear, but might be related to the onset of small scale convection.

Hence, there are complexities in thermal boundary layers beyond HSC that are apparent even in isotropic structure, and those can be expected to locally modify LPO formation. This also becomes apparent when age-referrencing the purely LPO-based ξ predictions of *Becker et al.* [2008], which, in fact, show flattening at ages of around 70 Ma (see bottom two panels in Fig. S6). Quantifying this effect via fiting the age dependent model given by eqns. (5) and (6) through the maximum ξ depths in the LPO model, we can infer slope and flattening parameters ($c = 2.2$, $f = 66$ Ma for the Pacific, and $c = 1.9$, $f = 75$ Ma for the Atlantic), which turn out to be very similar to the ones of model B in Fig. 2. This means that the age dependence of LPO models which include full dynamics and actual boundary layer structure [*Becker et al.*, 2008] is consistent with LPO formation. The average depth of the zone in the geodynamic LPO, however, model is generally deeper (150 km vs. 110 km for the Pacific, and 140 km vs. 80 km for the Atlantic; Fig. S6). This highlights, that

flattening itself is not per se an argument against an LPO origin of radial anisotropy. Yet, the depth discrepancy provides additional hint that pure LPO is not an ideal model for radial anisotropy. On the other hand, the LPO model's region where dislocation creep dominates and LPO forms is sensitive to the grain size [e.g. *Becker*, 2006; *Becker et al.*, 2008], which was chosen to roughly match older 1D average anisotropy profiles. Thus, it is conceivable, that improved LPO models may fall closer to the range of seismically admissible models, both in terms of age-dependence and depth of the layer.

Possible mismatch of LPO layer depths and the good correlation between the high-ξ zone and the subhorizontal SS and RF interface estimates, substantiate the results of *Burgos et al.* [2014], contrasting the clear age control that was found based on global and regional azimuthal anisotropy [*Becker et al.*, 2014]. We thus infer that additional mechanisms beyond purely thermal control within half-space cooling and A type LPO formation need to be invoked [*Beghein et al.*, 2014].

3.1. Partial melt, LPO or solid-state mechanisms

Temperature anomalies, such as the 80 Ma disturbance observed in the Pacific (Fig. 1c), are often associated with increased partial melting, and the presence of partial melt has been invoked as a possible geodynamic-petrological interpretation for the discrepancies discussed in sec. 3, at least locally [*Kawakatsu et al.*, 2009; *Schmerr*, 2012; *Beghein et al.*, 2014]. The shape preferred orientation induced radial anisotropy due to ubiquitous partial melt may itself be responsible for the impedance contrast observed in receiver functions [*Kawakatsu et al.*, 2009], and high partial melt fractions may also lead to LPO fabrics that are different from the A type expected for the background asthenosphere [*Holtzman*

et al., 2003; *Holtzman and Kendall*, 2010]. A higher degree of partial melting embedded in the lithosphere would be consistent with stronger radial anisotropy in the "hot" Pacific compared to the Atlantic (Table S1). However, even the simplified, A type LPO flow models of *Becker et al.* [2008] indicate stronger radial anisotropy underneath the Pacific, because of more efficient saturation of LPO, cautioning against the interpretation of peak anisotropy strength.

Moreover, *Karato* [2014] opposes the partial melt hypothesis, arguing that the amount of in-situ partial melt away from the ridge axis and hotspots does probably not exceed fractions of 0.1% and thus can neither result in a significant reduction in v_S nor explain the other observed geophysical anomalies [*Karato*, 2012, 2014]. Instead, *Karato* [2014] proposes the solid-state mechanism of anelastic relaxation based on grain boundary sliding, as an alternative explanation for high electrical conductivities and seismic anisotropy at nearly constant depth of 70 km.

In contrast, *Sakamaki et al.* [2013] have shown that melt density is highly pressure dependent, causing melt mobility to have a local maximum at depths between 120 and 150 km, coinciding with the range of strong anisotropy (Fig. 2). *Sakamaki et al.* [2013] suggest a tendency for partial melt ponding at the top of the asthenosphere, which, under shear deformation, may be reworked to sub-horizontal melt bands [e.g. *Holtzman and Kendall*, 2010]. If such melt formations cool down, an additional reduction in permeability would be expected [e.g. *Hirschmann*, 2010; *Hebert and Montési*, 2010]. A related mechanism has been described by *Sifre et al.* [2014], who show that CO^2-rich melting is

likely to occur in depths between $\sim$ 60 km and $\sim$ 150 km, with increased amounts of melt accumulation at a depth of around 70 km.

The degree to which partial melt is present and preserved in remnant SPO after cooling within the lithosphere is therefore unclear, and other petrological fabric alignment may at least contribute. The morphology of possible frozen-in melt-related structures or petrological layering may be further illuminated by the study of high-frequency, Po/So guided seismic wave arrivals [*Kennett and Furumura*, 2013]. *Kennett and Furumura* [2014] show that pervasive stochastic heterogeneities with horizontal and vertical correlation lengths of $\sim$ 10 km and $\sim$ 0.5 km, respectively, provide an explanation for such observations, and suggest that such petrological fabrics would manifest themselves in the form of seismic anisotropy.

3.2. Relation between anisotropy and interfaces

Our hypothesis-tests (Fig. 3) confirm that the weak to absent age-dependence in tomographically imaged ξ [*Burgos et al.*, 2014; *Beghein et al.*, 2014] is not a regularization artifact, and we interpret the association between the SS precursors and the top and the bottom of the radially anisotropic zone (Fig. 2) as due to a causal relationship. While the shallower discontinuity is relatively well described [e.g. *Rychert and Shearer*, 2011; *Kumar and Kawakatsu*, 2011; *Schmerr*, 2012], there are fewer observations of the deeper interface between 120 and 180 km. *Gaherty et al.* [1996] and *Gaherty et al.* [1999] observe an interface at comparable depth in their models $PA5$ and $PHB3$ and identify it with the oceanic incarnation of the Lehmann discontinuity, which is primarily observed underneath continents and there located at an average depth of $\sim$ 220 km. In the SS precursors,

the second interface is laterally even less continuous than the G, mostly connected with spreading centers or hotspots [*Schmerr*, 2012], and interpreted as being due to a negative velocity contrast (i.e. a drop in v_S with depth). Since SS precursors are horizontally polarized, an increase in anisotropy could also cause an impedance contrast. *Schmerr* [2012] shows that two types of velocity structures can produce synthetic waveforms similar to the observed ones: i), models comprising a negative velocity drop and, ii), models having a positive velocity increase or a positive gradient (implying that the weaker precursors would represent negative sidelobes of a weakly positive precursor). While (i) would be incompatible with a change from $v_{SH} > v_{SV}$ to $v_{SH} \approx v_{SV}$, (ii) would, in principle, agree with constraints from tomography. We infer that anisotropy may be a consequence of the same fabrics that are responsible for the observed seismic interfaces.

The question arises as to how a thermal interpretation of the lithosphere (Fig. 1) can be reconciled with observations of relatively shallower upper-mantle discontinuities. The assumption that receiver function estimates within oceanic plates mark the bottom of the lithosphere [e.g. *Kawakatsu et al.*, 2009; *Rychert and Shearer*, 2011] indeed motivated the designation of such impedance contrasts as the lithosphere-asthenosphere boundary (LAB). Instead, the shallow impedance contrasts and the G may in fact be due to partial melt or petrological fabrics within the mechanical oceanic lithosphere, i.e. a mid-lithospheric discontinuity (MLD) as reported widely for the continents [e.g. *Selway et al.*, 2015].

3.3. Conceptual interpretation

We propose the following model of the oceanic lithosphere (Fig. 4): Convective upwelling of mantle material leads to shallow decompression melting and basaltic crust formation under the spreading centers. Deeper in the mantle, partial melt accumulates in flow aligned, melt-rich channels, whose maximum depth is controlled by a reduction in melt mobility. This leads to lateral spreading of horizontal melt lamellae, which are eventually frozen into the lithosphere at roughly constant depth that is set by the asthenospheric temperature and spreading rate, with some degree of remelting [*Schmerr*, 2012].

A SPO type of radial anisotropy results, as suggested by *Kawakatsu et al.* [2009], which may alternatively be due to petrological fabrics. Mantle flow induced LPO contributes strongly to these shallow frozen-in structures at asthenospheric depths, again similar to what has been suggested for the continents [*Becker et al.*, 2008]. Frozen-in SPO will have a minor effect on azimuthal anisotropy if there is no preferred anisotropy of lamellae in the horizontal plane, and azimuthal anisotropy is therefore mainly sensitive to LPO due to shearing in the uppermost asthenosphere. The region of alignment between flow model predictions and observed azimuthal anisotropy marks the base of the mechanical lithosphere [*Becker et al.*, 2014].

4. Conclusions

Our experiments show that seismological-geodynamic hypotheses including a radially anisotropic layer with a strong age dependence achieve lower data fits than models which are weakly age-dependent. We infer that the observation of an radially anisotropic layer

that is bracketed by the two impedance contrasts is a robust feature, and due to a combination of mantle flow induced LPO and partial-melting or petrological fabric related SPO. While these interfaces provide information about the conditions under which oceanic plates are created, and perhaps remelted, the top, G, lies within the thermo-mechanically defined plate and is not of dynamical relevance.

Acknowledgments. We thank Domenico Giardini, John Hernlund and Marc Hirschmann for discussions, and Andreas Fichtner for providing computational resources via the Swiss National Supercomputing Centre (CSCS). TWB thanks ERI and Hitoshi Kawakatsu from the University of Tokyo for hosting him during a sabbatical where this work was initiated in 2011. Our work was supported by the Swiss National Fond (SNF) under grant number 2-77808-13 and NSF grants 1417993 and 1361325. Some of the figures have been prepared with GMT [*Wessel and Smith*, 1991].

References

Auer, L., L. Boschi, T. W. Becker, T. Nissen-Meyer, and D. Giardini (2014), Savani: A variable-resolution whole-mantle model of anisotropic shear-velocity variations based on multiple datasets, *J. Geophys. Res.*, *119*, 3006–3034, doi:10.1002/2013JB010773.

Bassin, C., G. Laske, and G. Masters (2000), The current limits of resolution for surface wave tomography in North America (abstract), *Eos Trans. AGU*, *81*, F897.

Becker, T. W. (2006), On the effect of temperature and strain-rate dependent viscosity on global mantle flow, net rotation, and plate-driving forces, *Geophys. J. Int.*, *167*, 943–957.

Becker, T. W., S. Chevrot, V. Schulte-Pelkum, and D. K. Blackman (2006), Statistical properties of seismic anisotropy predicted by upper mantle geodynamic models, *J. Geophys. Res.*, *111*(B08309), doi:10.1029/2005JB004095.

Becker, T. W., B. Kustowski, and G. Ekström (2008), Radial seismic anisotropy as a constraint for upper mantle rheology, *Earth Planet. Sci. Lett.*, *267*, 213–237, doi:10.1016/j.epsl.2007.11.038.

Becker, T. W., C. P. Conrad, A. Schaeffer, and S. Lebedev (2014), Origin of azimuthal seismic anisotropy in oceanic plates and mantle, *Earth Planet. Sci. Lett.*, *402*, 236–250, doi:10.1016/j.epsl.2014.06.014.

Beghein, C., K. Yuan, N. Schmerr, and Z. Xing (2014), Changes in seismic anisotropy shed light on the nature of the Gutenberg discontinuity, *Science*, *343*, 1237–1240, doi:10.1126/science.1246724.

Boschi, L., and A. M. Dziewoński (1999), 'High' and 'low' resolution images of the Earth's mantle – Implications of different approaches to tomographic modeling, *J. Geophys. Res.*, *104*, 25,567–25,594, doi:10.1029/1999JB900166.

Boschi, L., and G. Ekström (2002), New images of the Earth's upper mantle from measurements of surface-wave phase velocity anomalies, *J. Geophys. Res.*, *107*, doi:10.1029/2000JB000059.

Burgos, G., J.-P. Montagner, E. Beucler, Y. Capdeville, A. Mocquet, and M. Drilleau (2014), Oceanic lithosphere/asthenosphere boundary from surface wave dispersion data, *J. Geophys. Res.*, pp. 1079–1093, doi:10.1002/2013JB010528.

Chen, K., and P. Molnar (1983), Focal depths of intracontinental and intraplate earthquakes and their implications for the thermal and mechanical properties of the lithosphere, *J. Geophys. Res.*, *88*, 4183–4214.

Dalton, C. A., C. H. Langmuir, and A. Gale (2014), Geophysical and geochemical evidence for deep temperature variations beneath mid-ocean ridges, *Science*, *344*, 80–83, doi: 10.1126/science.1249466.

Dziewoński, A. M., and D. L. Anderson (1981), Preliminary reference Earth model, *Phys. Earth Planet. Inter.*, *25*, 297–356.

Ekström, G. (2011), A global model of love and rayleigh surface wave dispersion and anisotropy, 25-250s, *Geophys. J. Int.*, *187*, 1668–1686.

Ekström, G., and A. M. Dziewonski (1998), The unique anisotropy of the Pacific upper mantle, *Nature*, *394*, 168–172, doi:10.1038/28148.

French, S., V. Lekić, and B. Romanowicz (2013), Waveform tomography reveals channeled flow at the base of the oceanic asthenosphere, *Science*, *342*, 227–230, doi: 10.1126/science.1241514.

Gaherty, J. B., T. H. Jordan, and L. S. Gee (1996), Seismic structure of the upper mantle in a central Pacific corridor, *J. Geophys. Res.*, *101*, 22,291–22,310, doi:10.1029/96JB01882.

Gaherty, J. B., M. Kato, and T. H. Jordan (1999), Seismological structure of the upper mantle: a regional comparison of seismic layering, *Phys. Earth Planet. Inter.*, *110*, 21–41, doi:10.1016/S0031-9201(98)00132-0.

Gutenberg, B. (1926), Untersuchungen zur Frage, bis zu welcher Tiefe die Erde kristallin ist, *Zeitschr. Geophys.*, *2*, 24–29.

Hansen, L. N., M. E. Zimmerman, and D. L. Kohlstedt (2014), Protracted fabric evolution in olivine: Implications for the relationshipamong strain, crystallographic fabric, and seismic anisotropy, *EPSL*, *387*, 157–168, doi:10.1016/j.epsl.2013.11.009.

Hebert, L. B., and L. G. J. Montési (2010), Generation of permeability barriers during melt extraction at mid-ocean ridges, *Geochem., Geophys., Geosys.*, *11*(12), doi:10.1029/2010GC003270.

Hirschmann, M. H. (2010), Partial melt in the oceanic low velocity zone, *Phys. Earth Planet. Inter.*, *179*, 60–71, doi:10.1016/j.pepi.2009.12.003.

Holtzman, B. K., and J. Kendall (2010), Organized melt, seismic anisotropy, and plate boundary lubrication, *Geochem., Geophys., Geosys.*, *11*(Q0AB06), doi:10.1029/2010GC003296.

Holtzman, B. K., D. L. Kohlstedt, M. E. Zimmerman, F. Heidelbach, T. Hiraga, and J. Hustoft (2003), Melt segregation and strain partitioning: Implications for seismic anisotropy and mantle flow, *Science*, *301*, 1227–1230.

Huang, J., and S. Zhong (2005), Sublithospheric small-scale convection and its implications for the residual topography at old ocean basins and the plate model, *J. Geophys. Res.*, *110*(B05404), doi:10.1029/2004JB003153.

Karato, S.-i. (2012), On the origin of the asthenosphere, *Earth Planet. Sci. Lett.*, *321–322*, 95–103, doi:10.1016/j.epsl.2012.01.001.

Karato, S.-i. (2014), Does partial melting explain geophysical anomalies?, *Phys. Earth Planet. Inter.*, *228*, 300–306, doi:10.1016/j.pepi.2013.08.006.

448 Karato, S.-i., H. Jung, I. Katayama, and P. Skemer (2008), Geodynamic signficance of
449 seismic anisotropy of the upper mantle: new insights from laboratory studies, *Ann Rev.*
450 *Earth Planet. Sci.*, *36*, 59–95, doi:10.1146/annurev.earth.36.031207.124120.

451 Kawakatsu, H., P. Kumar, Y. Takei, M. Shinohara, T. Kanazawa, E. Araki, and K. Suye-
452 hiro (2009), Seismic Evidence for Sharp Lithosphere-Asthenosphere Boundaries of
453 Oceanic Plates, *Science*, *324*, 499–502, doi:10.1126/science.1169499.

454 Kennett, B. L. N., and T. Furumura (2013), High-frequency Po/So guided waves in the
455 oceanic lithosphere: I − long-distance propagation, *Geophys. J. Int.*, *195*, 1862–1877,
456 doi:10.1093/gji/ggt344.

457 Kennett, B. L. N., and T. Furumura (2014), High-frequency Po/So guided waves in the
458 oceanic lithosphere: II − heterogeneity and attenuation, *Geophys. J. Int.*, *199*, 614–630,
459 doi:10.1093/gji/ggu286.

460 Kumar, P., and H. Kawakatsu (2011), Imaging the seismic lithosphere-asthenosphere
461 boundary of the oceanic plate, *Geochem., Geophys., Geosys.*, *12*(Q01006), doi:
462 10.1029/2010GC003358.

463 Kustowski, B., G. Ekström, and A. M. Dziewoński (2008), Anisotropic shear-wave ve-
464 locity structure of the Earth's mantle: A global model, *J. Geophys. Res.*, *113*, doi:
465 10.1029/2007JB005169.

466 Long, M. D., and T. W. Becker (2010), Mantle dynamics and seismic anisotropy, *Earth*
467 *Planet. Sci. Lett.*, *297*, 341–354, doi:10.1016/j.epsl.2010.06.036.

468 Marty, J. C., and A. Cazenave (1989), Regional variations in subsidence rate of oceanic
469 plates: a global analysis, *Earth Planet. Sci. Lett.*, *94*, 301–315.

McKenzie, D., J. Jackson, and K. Priestley (2005), Thermal structure of oceanic and continental lithosphere, *Earth Planet. Sci. Lett.*, *233*, 337–349, doi: 10.1016/j.epsl.2005.02.005.

Müller, R. D., M. Sdrolias, C. Gaina, and W. R. Roest (2008), Age, spreading rates and spreading asymmetry of the world's ocean crust, *Geochem., Geophys., Geosys.*, *9*(Q04006), doi:10.1029/2007GC001743.

Nagihara, S., C. R. B. Lister, and J. G. Sclater (1996), Reheating of old oceanic lithosphere: Deductions from observations, *Earth Planet. Sci. Lett.*, *139*, 91–104, doi: 10.1016/0012-821x(96)00010-6.

Nettles, M., and A. M. Dziewoński (2008), Radially anisotropic shear-velocity structure of the upper mantle globally and beneath North America, *J. Geophys. Res.*, *113*(B02303), doi:10.1029/2006JB004819.

Priestley, K., and D. McKenzie (2013), The relationship between shear wave velocity, temperature, attenuation and viscosity in the shallow part of the mantle, *Earth Planet. Sci. Lett.*, *381*, 78–91.

Ritzwoller, M. H., N. M. Shapiro, and S. Zhong (2004), Cooling history of the Pacific lithosphere, *Earth Planet. Sci. Lett.*, *226*, 69–84, doi:10.1016/j.epsl.2004.07.032.

Rychert, C. A., and P. M. Shearer (2011), Imaging the lithosphere-asthenosphere boundary beneath the Pacific using SS waveform modeling, *J. Geophys. Res.*, *116*(B07307), doi:10.1029/2010JB008070.

Rychert, C. A., N. Schmerr, and N. Harmon (2012), The Pacific lithosphere-asthenosphere boundary: Seismic imaging and anisotropic constraints from SS waveforms, *Geochem.,*

Geophys., Geosys., *13*(Q0AK10), doi:10.1029/2012GC004194.

Sakamaki, T., A. Suzuki, E. Ohtani, H. Terasaki, S. Urakawa, Y. Katayama, K.-i. Funakoshi, Y. Wang, J. W. Hernlund, and M. D. Ballmer (2013), Ponded melt at the boundary between the lithosphere and asthenosphere, *Nature Geosc.*, *6*, 1041–1044, doi:10.1038/NGEO1982.

Schmerr, N. (2012), The Gutenberg discontinuity: Melt at the lithosphere-asthenosphere boundary, *Science*, *335*, 1480–1483, doi:10.1126/science.1215433.

Selway, K., H. Ford, and P. Keleman (2015), The seismic mid-lithosphere discontinuity, *Earth Planet. Sci. Lett.*, *414*, 45–57, doi:10.1016/j.epsl.2014.12.029.

Sifre, D., E. Gardes, M. Massuyeau, L. Hashim, S. Hier-Majumder, and F. Gaillard (2014), Electrical conductivity during incipient melting in the oceanic low-velocity zone, *Nature*, *85*, 81–85, doi:10.1038/nature13245.

Tarantola, A. (2006), Popper, Bayes and the inverse problem, *Nat. Phys.*, *2*, 492–494.

Turcotte, D. L., and G. Schubert (2002), *Geodynamics*, 2 ed., Cambridge University Press, Cambridge.

Watts, A. B., J. Hunter, and S. S. J. Zhong (2013), The behavior of the lithosphere on seismic to geologic timescales, *Ann. Rev. Earth Planet. Sci.*, *41*, 443–468, doi:10.1146/annurev-earth-042711-105457.

Wessel, P., and W. H. F. Smith (1991), Free software helps map and display data, *Eos Trans. AGU*, *72*, 445–446, doi:10.1029/90EO00319.

Zhong, S., M. Ritzwoller, N. Shapiro, W. Landuyt, J. Huang, and P. Wessel (2007), Bathymetry of the Pacific plate and its implications for thermal evolution of lithosphere

514 and mantle dynamics, *J. Geophys. Res.*, *112*(B06412), doi:10.1029/2006JB004628.

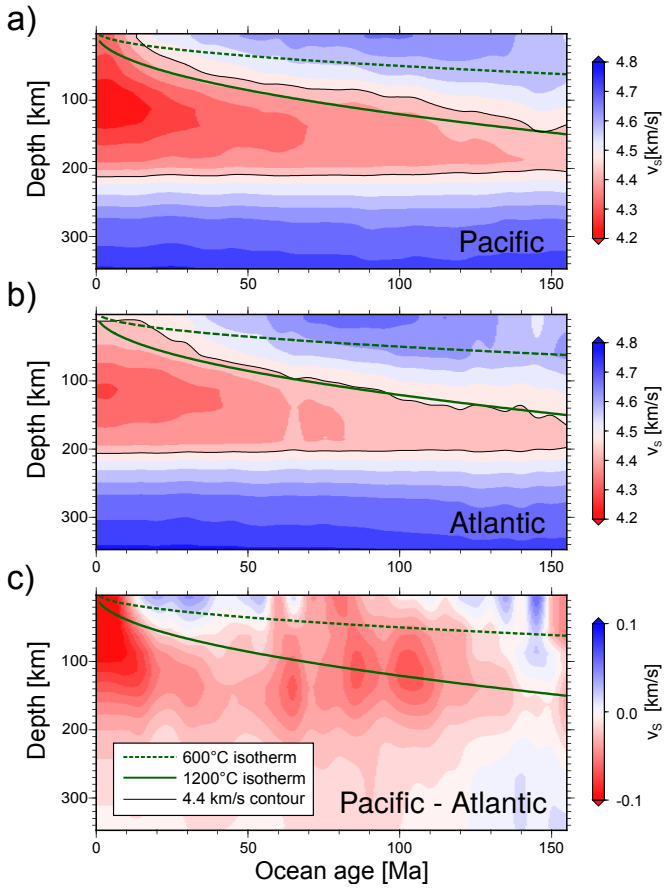

Figure 1. Isotropic Voigt velocities as imaged by the anisotropic tomography *savani* [*Auer et al.*, 2014], referenced against sea-floor age from *Müller et al.* [2008]. For the Pacific (a) deviations from the simple half-space cooling description are observed, while for Atlantic Ocean (b) a simple-half space cooling provides a reasonable explanation: the 1200°C isotherm from temperature-dependent conductivity models [cf. *McKenzie et al.*, 2005] loosely follows the 4.4 km/s isoline and confines an underlying low velocity zone. The Pacific anomaly is illustrated in the difference plot (c) where the Atlantic was subtracted from the Pacific results.

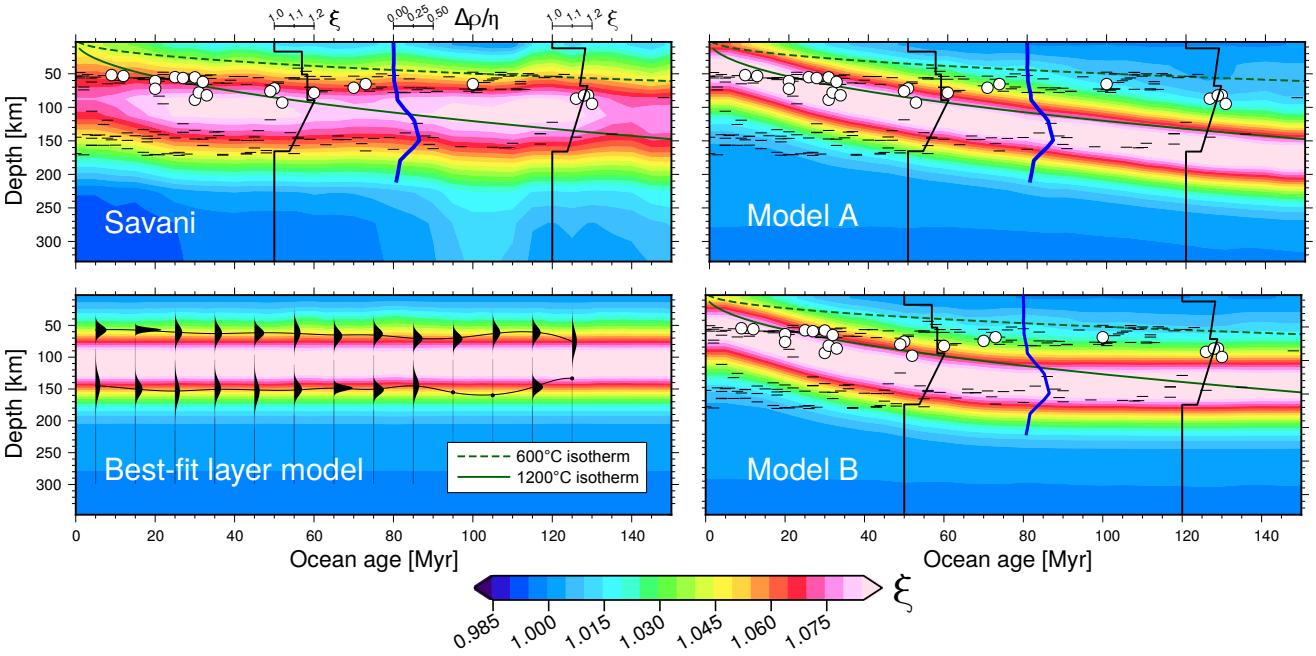

Figure 2. Top left panel: Radial anisotropy from *savani* [*Auer et al.*, 2014], $\xi = (v_{SH}/v_{SV})^2$, referenced against sea-floor age [*Müller et al.*, 2008] underneath the Pacific. Note how the high ξ zone is nearly independent of sea-floor age [*Burgos et al.*, 2014; *Beghein et al.*, 2014], its top coincides with the receiver function estimate of the Gutenberg discontinuity [*Kumar and Kawakatsu*, 2011] (white dots), and its top and bottom coincide with *SS* precursor based discontinuities [*Schmerr*, 2012] (black strokes). The depth bracket also matches a peak in melt mobility [*Sakamaki et al.*, 2013] (blue line, indicating density anomaly, $\Delta\rho$, divided by inferred viscosity, η, from a simple thermal model). Bottom left panel: Best-fit layer model for the Pacific; interface depths are represented via black histograms. Right panels: Selected strongly (A) and weakly (B) age-dependent models.

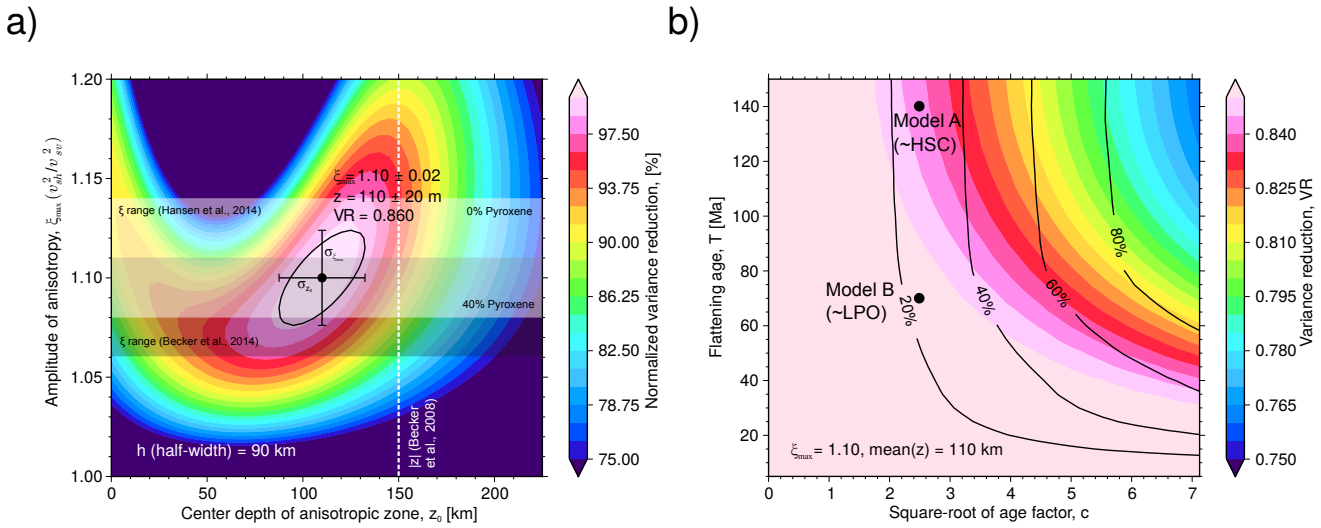

Figure 3. a) Variance reductions for the Pacific data subset, illuminating depth-vs.-anisotropy strength trade-offs and best fit parameter ranges in the case where the anisotropic layer is represented with an age-independent Gaussian. The dark and the white zones represent the geodynamic and experimental LPO predictions of peak radial anisotropy strength, from *Becker et al.* [2008] (Fig. S6) and *Hansen et al.* [2014], respectively, for regular A type fabrics, and the white dashed line is the average peak depth from *Becker et al.* [2008]. b) Variance reductions in the case where we dial between age-dependent and flat-layer type conceptual models. There is some preference for entirely age-independent models and models that flatten out at young ages (e.g. model B) over models that follow the geodynamically meaningful isotherms (such as the 1200°C isotherm, e.g. model A). The black isocontours mark the normalized roughness associated with each model and show that the completely age-independent models are also the smoothest models.

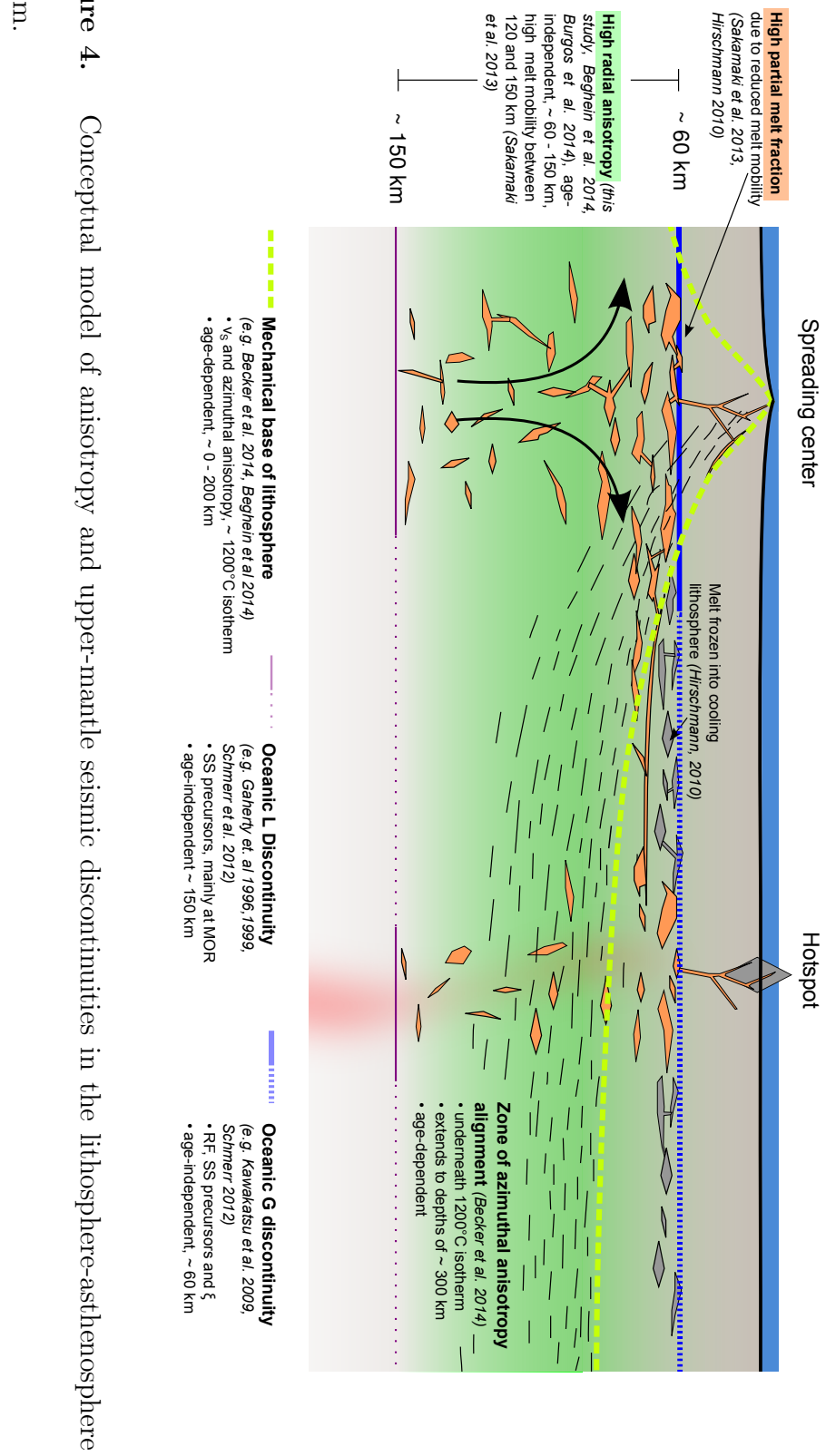

Figure 4. Conceptual model of anisotropy and upper-mantle seismic discontinuities in the lithosphere-asthenosphere system.